Aalto University School of Engineering
CFD-group/ Department of Applied Mechanics

MEMO No CFD/MECHA-7-2011 DATE: January 21, 2011

TITLE

Study of Simulation Parameters and Flow-Controlled Boundary Conditions in a Single-Blade Pump Simulation

AUTHOR(S)
Juhaveikko Ala-Juusela

ABSTRACT

A single-blade sewage pump is simulated numerically using a FINFLO flow-solver. Low-Reynolds number approach is utilized with a $k-\epsilon$ turbulence closure. Influence of an internal timestep on a convergence of a time-accurate simulation is studied. The effect of the boundary conditions on a performance prediction, mass balance fluctuation and velocity distributions is studied by using also flow controlled boundary conditions.

MAIN RESULT

Pump head, efficiency and torque are obtained from the simulated flowfield and compared to measured data. The velocity distributions are also compared to the measurements available. The convergence of the pressure is poor witch affects significantly pump performance prediction. In spite of that, prediction of velocity distributions is quite good.

PAGES
33

KEY WORDS
FINFLO, $k-\epsilon$ model, pump performance, chimera, periodic

APPROVED BY

Timo Siikonen January 21, 2011

Contents

Nomenclature

C_p	pressure coefficient
E	total energy
F, G, H	flux vectors in the x-, y- and z-directions
H	total head
Pr	Prandtl number
Q	source term vector
Re	Reynolds number
T	temperature
U	vector of conservative variables
V	velocity vector
c_p	specific heat at a constant pressure
c_v	specific heat at a constant volume
e	specific internal energy
k	turbulent kinetic energy
$\dot{m}$	mass flow
p	pressure
$\vec{q}$	heat flux
t	time
u, v, w	velocity components in the x-, y- and z-directions
u_τ	friction velocity ($= \sqrt{\tau_w/\rho}$)
y^+	dimensionless distance from the wall ($= yu_\tau/\nu$)
β	artificial compressibility coefficient
δ_{ij}	Kronecker's delta
ϵ	dissipation of the kinetic energy of the turbulence
θ	temperature difference ($= T - T_\infty$)
μ	dynamic viscosity
ν	kinematic viscosity
ϕ	scalar
ρ	density
τ	shear stress

Superscripts

T	transposition
l	left side
r	right side
w	wall value
$'$	fluctuating component

Subscripts

T	turbulent
i, j, k	i-, j- and k-component
t	tangential component
n	normal component

1 Introduction

In this study a single-blade sewage pump is simulated numerically using FINFLO flow solver. A low-Reynolds number $k-\epsilon$ turbulence model is utilized in the simulations. The case has been simulated earlier using the velocity as an inlet and the pressure as an outlet boundary condition [1]. Since in this approach there were severe oscillations in the mass flow, in this study number of internal iterations in time-dependent simulation is increased. This was done in order to get a fully converged result at every time step. Furthermore, boundary conditions are replaced either by placing the pump in a test tank utilizing overlapping grid method or by utilizing periodic boundary conditions. The flow is controlled by changing the area of exhaust pipe cross section, in a similar manner as using a trottle valve.

In the following, the governing equations and turbulence modelling are firstly described. Next, the computational domain and the grid are depicted and, finally, the results of the simulation are presented and compared to measurements as well as previous simulations with the different boundary condition approach.

2 Flow Equations

A low-Reynolds number approach is used in FINFLO. The Reynolds-averaged Navier-Stokes equations, and the equations for the kinetic energy (k) and dissipation (ϵ) of turbulence can be written in the following form

$$\frac{\partial U}{\partial t}+\frac{\partial(F-F_v)}{\partial x}+\frac{\partial(G-G_v)}{\partial y}+\frac{\partial(H-H_v)}{\partial z}=Q \tag{1}$$

where the unknowns are $U=(\rho,\rho u,\rho v,\rho w,E,\rho k,\rho\epsilon)^T$. The inviscid fluxes are

$$F=\begin{pmatrix}\rho u\\ \rho u^2+p+\frac{2}{3}\rho k\\ \rho vu\\ \rho wu\\ (E+p+\frac{2}{3}\rho k)u\\ \rho uk\\ \rho u\epsilon\end{pmatrix}\quad G=\begin{pmatrix}\rho v\\ \rho uv\\ \rho v^2+p+\frac{2}{3}\rho k\\ \rho wv\\ (E+p+\frac{2}{3}\rho k)v\\ \rho vk\\ \rho v\epsilon\end{pmatrix}\quad H=\begin{pmatrix}\rho w\\ \rho uw\\ \rho vw\\ \rho w^2+p+\frac{2}{3}\rho k\\ (E+p+\frac{2}{3}\rho k)w\\ \rho wk\\ \rho w\epsilon\end{pmatrix} \tag{2}$$

where ρ is the density, the velocity vector by using Cartesian components is $\vec{V}=u\vec{i}+v\vec{j}+w\vec{k}$, p is the pressure, k is the turbulent kinetic energy and ϵ its dissipation, and the total energy E is defined as

$$E=\rho e+\frac{\rho\vec{V}\cdot\vec{V}}{2}+\rho k \tag{3}$$

where e is the specific internal energy. The viscous fluxes are

$$F_v = \begin{pmatrix} 0 \\ \tau_{xx} \\ \tau_{xy} \\ \tau_{xz} \\ u\tau_{xx} + v\tau_{xy} + w\tau_{xz} - q_x \\ \mu_k(\partial k/\partial x) \\ \mu_\epsilon(\partial \epsilon/\partial x) \end{pmatrix} G_v = \begin{pmatrix} 0 \\ \tau_{xy} \\ \tau_{yy} \\ \tau_{yz} \\ u\tau_{xy} + v\tau_{yy} + w\tau_{yz} - q_y \\ \mu_k(\partial k/\partial y) \\ \mu_\epsilon(\partial \epsilon/\partial y) \end{pmatrix}$$

$$H_v = \begin{pmatrix} 0 \\ \tau_{xz} \\ \tau_{yz} \\ \tau_{zz} \\ u\tau_{xz} + v\tau_{yz} + w\tau_{zz} - q_z \\ \mu_k(\partial k/\partial z) \\ \mu_\epsilon(\partial \epsilon/\partial z) \end{pmatrix} \tag{4}$$

Here the stress tensor, τ_{ij}, includes laminar and turbulent components. The fluid is assumed to be Newtonian and, therefore, the laminar stresses are modelled by using Stokes hypothesis. The Reynolds stresses $\overline{\rho u_i'' u_j''}$ are included in the stress tensor τ_{ij}.

$$\tau_{ij} = \mu \left[\frac{\partial u_j}{\partial x_i} + \frac{\partial u_i}{\partial x_j} - \frac{2}{3}(\nabla \cdot \vec{V})\delta_{ij} \right] - \overline{\rho u_i'' u_j''} + \frac{2}{3}\rho k \delta_{ij} \tag{5}$$

For the Reynolds stresses, Boussinesq's approximation

$$-\overline{\rho u_i'' u_j''} = \mu_T \left[\frac{\partial u_j}{\partial x_i} + \frac{\partial u_i}{\partial x_j} - \frac{2}{3}(\nabla \cdot \vec{V})\delta_{ij} \right] - \frac{2}{3}\rho k \delta_{ij} \tag{6}$$

is utilized. Here μ_T is a turbulent viscosity coefficient, which is calculated by using a turbulence model, and δ_{ij} is the Kronecker's delta. In the momentum and energy equations, the kinetic energy contribution $2/3\rho k\delta_{ij}$ has been connected with pressure and appears in the convective fluxes, whereas the diffusive part is connected with the viscous fluxes. The viscous stresses contains a laminar and a turbulent parts. The heat flux can be written as

$$\vec{q} = -(\lambda + \lambda_T)\nabla T = -\left(\mu \frac{c_p}{Pr} + \mu_T \frac{c_p}{Pr_T} \right) \nabla T \tag{7}$$

where λ is a molecular and λ_T a turbulent thermal conductivity coefficient and Pr is a laminar and Pr_T a turbulent Prandtl number, and c_p is a specific heat at constant pressure. The diffusion of turbulence variables is modelled as

$$\mu_k \nabla k = \left(\mu + \frac{\mu_T}{\sigma_k} \right) \nabla k \tag{8}$$

$$\mu_\epsilon \nabla\epsilon = \left(\mu + \frac{\mu_T}{\sigma_\epsilon}\right)\nabla\epsilon \tag{9}$$

where σ_k and σ_ϵ are turbulent Schmidt's numbers of k and ϵ, respectively. Density is obtained from an equation of state $p = p(\rho, T)$ Since this case is essentially incompressible, pressure differences $p - p_0$ are solved instead of pressure. The components of the source term Q are non-zero in possible buoyancy terms and in turbulence model equations. In this study the buoyancy terms are insignificant and not applied.

In the present study an artificial compressibility approach is used to determine the pressure. The flux calculation is a simplified version of the approximate Riemann-solver utilized for compressible flows [2]. It should be noted that in this approach the artificial sound speed affects the solution, but the effect is of the second-order and it should not be visible as the grid is refined. The effect is similar to the Rhie and Chow interpolation method applied in commercial codes. The solution method applied is described in [3]. In time-accurate simulations the artificial compressibility approach is used inside a physical time step [4]. Each time step is treated as a steady-state case and iterations are made inside the time step. The time derivative term is treated as a source term. The method is fully implicit and a three-level approximation is used for the time derivative.

3 Turbulence Modelling

As mentioned, turbulent stresses resulting from the Reynolds averaging of the momentum equation are modelled by using Boussinesq's approximation (6). The turbulent viscosity coefficient μ_T is determined by using Chien's [5] low-Reynolds number $k - \epsilon$ model from the formula

$$\mu_T = c_\mu \rho \frac{k^2}{\epsilon} \tag{10}$$

where c_μ is a empirical coefficient. The source term of Chien's model is

$$Q = \begin{pmatrix} P - \rho\epsilon - 2\mu\dfrac{k}{y_n^2} \\ c_1\dfrac{\epsilon}{k}P - c_2\dfrac{\rho\epsilon^2}{k} - 2\mu\dfrac{\epsilon}{y_n^2}e^{-y^+/2} \end{pmatrix} \tag{11}$$

where y_n is the normal distance from the wall, and the dimensionless distance y^+ is defined by

$$y^+ = y_n\frac{\rho u_\tau}{\mu} = y_n\frac{\sqrt{\rho\tau_w}}{\mu} \approx y_n\left[\frac{\rho|\nabla\times\vec{V}|}{\mu}\right]_w^{1/2} \tag{12}$$

Here u_τ is friction velocity and τ_w is friction on the wall, and the connection between them is $u_\tau = \sqrt{\tau_w/\rho}$. The unknown production of the turbulent

kinetic energy is modelled using Boussinesq's approximation (6)

$$\begin{aligned} P &= -\overline{\rho u_i'' u_j''}\frac{\partial u_i}{\partial x_j} \\ &= \left[\mu_T(\frac{\partial u_i}{\partial x_j}+\frac{\partial u_j}{\partial x_i}-\frac{2}{3}\delta_{ij}\frac{\partial u_k}{\partial x_k})-\frac{2}{3}\delta_{ij}\rho k\right]\frac{\partial u_i}{\partial x_j} \end{aligned} \tag{13}$$

The turbulence model presented above contains empirical coefficients. Those are given by [2]

$$\begin{array}{lllllll} c_1 &=& 1.44 & & \sigma_k &=& 1.0 \\ c_2 &=& 1.92(1-0.22e^{-Re_T^2/36}) & & \sigma_\epsilon &=& 1.3 \\ c_\mu &=& 0.09(1-e^{-0.0115y^+}) & & & & \end{array} \tag{14}$$

where the turbulence Reynolds number is defined as

$$Re_T = \frac{\rho k^2}{\mu\epsilon} \tag{15}$$

Chien's model is very robust, but it has several shortcomings. It usually overestimates the turbulence level and is not performing well in a case of an increasing pressure gradient. However, in the present study the main emphasis is to study the behaviour of the numerical method, where turbulence plays a minor role.

4 Computational Grids and Boundary Conditions

All computational grids are based on grid that is described in detail in reference [1]. Only the second grid level (every other gridpoint) is used in this simulation, since the main purpose is to study the effect of boundary conditions and grid converged results are not important.

4.1 Fixed Velocity

The massflow of this case is 33 kg/s. A quasi-steady simulation is used as a starting guess for the time-accurate simulation. Velocity and turbulence quantities are used as a pump inlet boundary condition and the pressure is given as the pump outlet boundary condition.

4.2 Test Tank

In test tank case the pump grid is placed inside retangular tank. The tank grid is quite coarse, but is clustered around pumps inlet and outlet area. Clustering is necessary for the Chimera interpolation method, where the Chimera and

backround grids should have about same density. In this simulation the total number of grid cells is 403 072. There are 162 944 grid cells in the impeller part of the grid, 111 104 in the volute part and 129 024 in the tank part. The surface grid is depicted in Fig. 1.

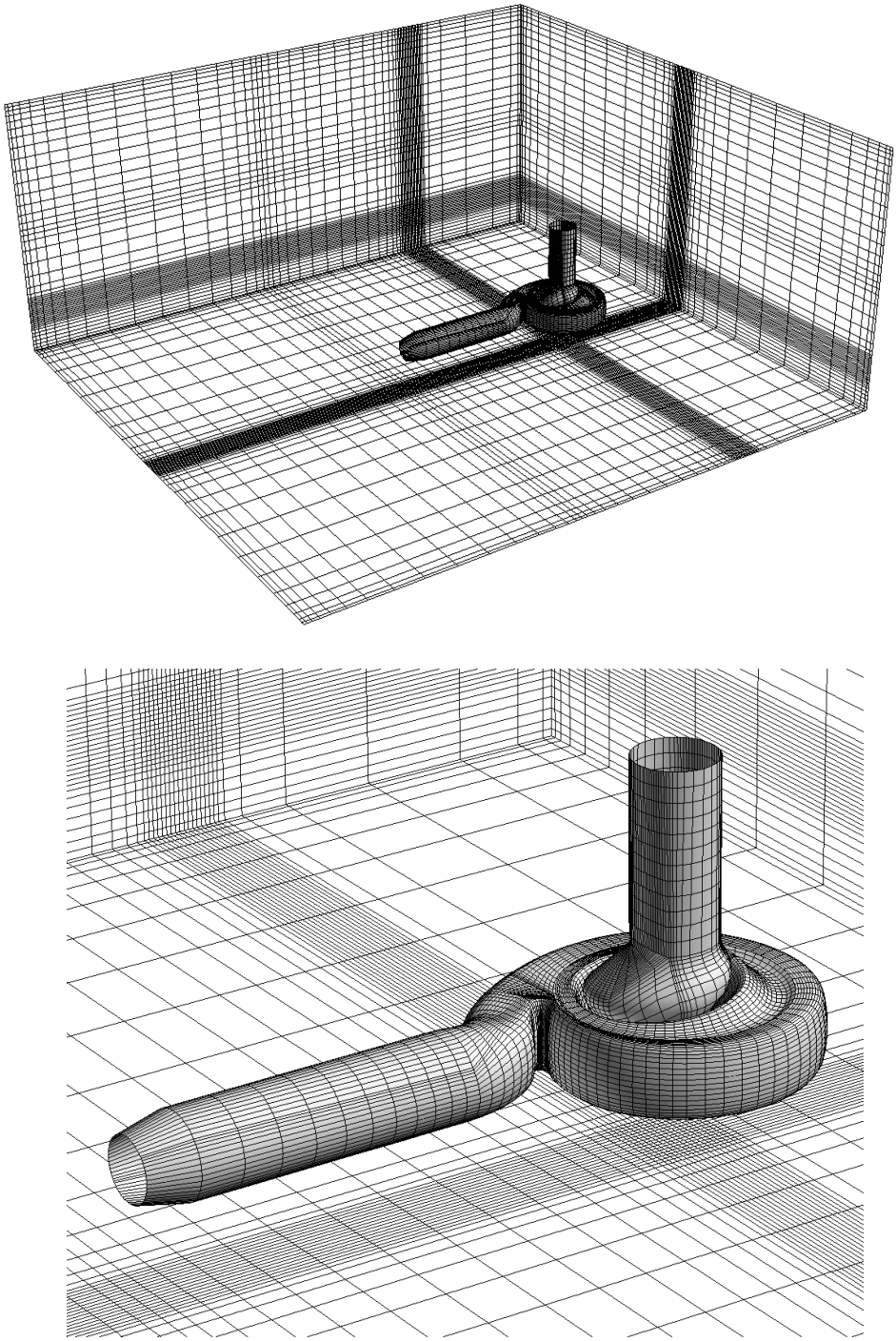

Fig. 1: Surface grid of tank and the pump.

Also in this case a quasi-steady simulation is used as a starting guess for the time-accurate simulation. The quasi-steady simulation is started using velocity and turbulence quantities as a pump inlet boundary condition and the pressure is given as the pump outlet boundary condition. A value of 800 000 Pa is given for the outlet pressure in order to prevent negative pressures during the iteration. The pressure level is insignificant in a present incompressible case. As the flow through the pump is established, the inlet and outlet boundary conditions are changed to overlapping boundaries. Since the flow is not regulated by the boundary condition, the area of the outlet surface has to be adjusted in order to get a correct massflow. The diameter of the outlet is reduced from from 100 mm to 80 mm, thus the area is reduced by 38.5 %. In the quasi steady simulation the massflow was 29 kg/s, but during the time accurate simulation massflow changed to 32 kg/s, which was considered to be close enought the massflow used in other simulations.

4.3 Periodic Loop

This grid is same as pump part in test tank simulation, except the outlet pipe is extended and, because of the implementation of periodic boundary condition in FINFLO, it is bended down. Also there is a non-matching surface after the bend, since the periodic boundary condition needs to have a same grid distribution in both ends. The total number of grid cells is 295 808, there are 21 760 cells in the added duct. The surface grid is depicted in Fig. 2.

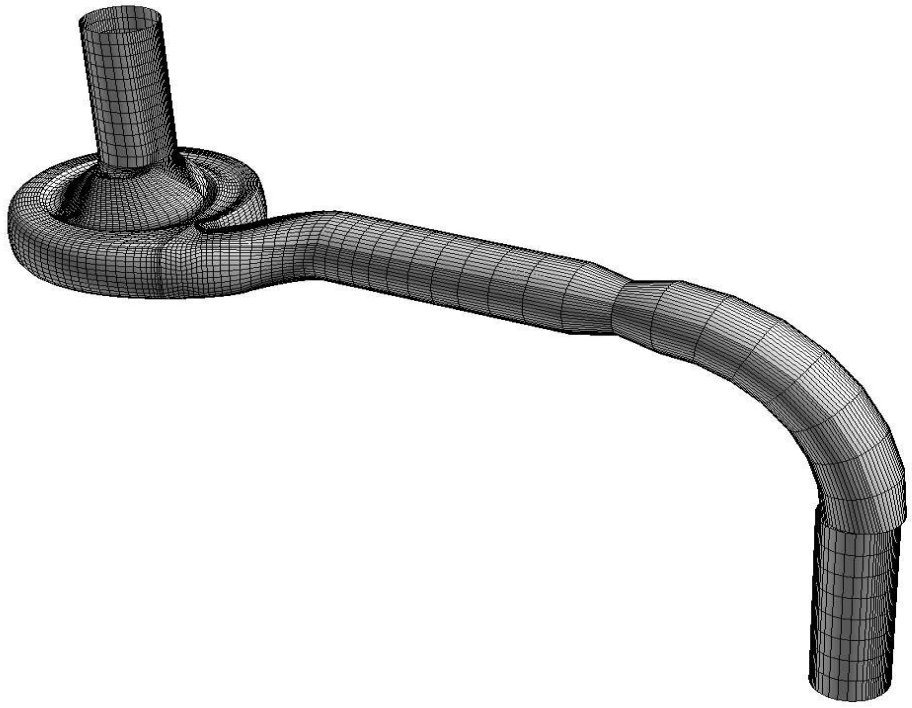

Fig. 2: Surface grid of a periodic loop pump.

5 Results

A quasi-steady simulation was used as as an initial guess for the time-accurate simulations. With the inlet/outlet boundary conditions, eight impeller revolutions were simulated with 200 internal iterations, after that four revolutions with as much as 2000 iterations.

With the tank case five impeller revolutions and with the pipe loop case seven revolutions were simulated. In the both of these simulations, 200 internal iterations are used for two first impeller rounds and 400 iterations after that. The Courant number of the internal iterations is equal to one in all simulations.

A multigrid acceleration could not be used to accelerate convergence in the time-accurate simulations due to unknouwn instability, in the quasi-stedy computations two multi-grid layers were used.

Unfortunately the pipe loop case results suffer from the fact that non-matching boundary is reducing the time-dependent nature of the flow. In Fig. 3 massflows at upstream and downstream sides of non-matching connection and at periodic inlet and outlet are shown. It can be seen that there is also a small difference in massflows between periodic inlet and outlet but amplidude is in sama phase and magnitude. Since massflow remains constant over non-maching connection in quasi-steady simulation, the problem is extremely difficult and could not be solved within this study.

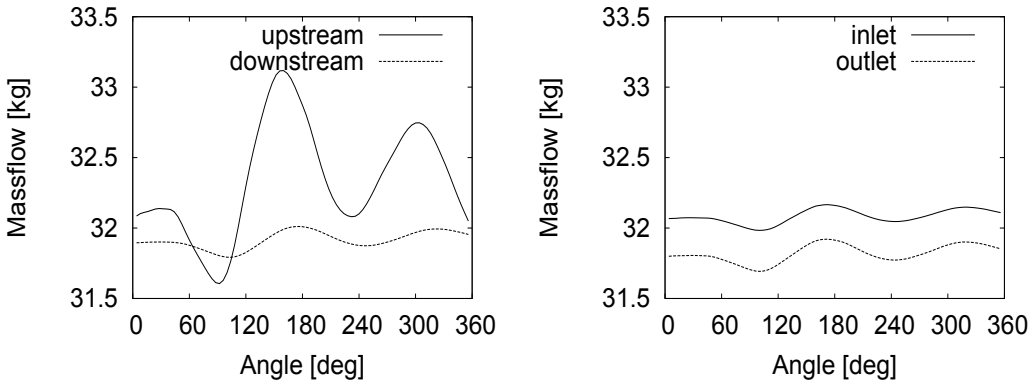

Fig. 3: Massflows at upstream and downstream side of the non-matching connection (left) and at periodic inlet and outlet (right).

A head is calculated from

$$H = \frac{p_2 - p_1}{\rho g} \tag{16}$$

where p_1 is the inlet pressure, p_2 the outlet pressure; ρ the density, and g the acceleration due to gravity. The efficiency is obtained from

$$\eta = \Delta E / T\omega \tag{17}$$

where ΔE is the difference between the mechanical energy flux at the inlet and the outlet and $T\omega$ is the required axial power. The axial power should

be smaller than the measured one, since several components of the loss, for example the friction on the outside of the impeller and bearing losses, are not taken into account. The head, efficiency and axial power needed are presented in Table 1. The test tank and pipe loop cases are compared the to the standard fixed velocity inlet and fixed pressure outlet case, which are simulated using 200 and 2 000 internal iterations.

Table. 1: Pump performance.

Case	Total Head	Efficiency	Shaft Power
Inlet/outlet 200	12.95 m	82.4%	5289 W
Inlet/outlet 2000	13.2 m	80.3%	5857 W
Test tank	12.53 m	62.1%	5593 W
Pipe loop	9.1 m	64.6%	5457 W
Experimental	12.4 m	71.1 %	5675 W

The head, mass balance, efficiency and axial power over a one impeller cycle are shown in Figs. 4 – 5. It can be seen, that fixed velocity with 200 internal iterations cause heavy oskillation in head value, as well as in outlet massflow and efficiency. Increasing number of internal iterations reduces maximum amplitude but in turn it produces high-frequency oscillations instead of the original sinusoidal head curve. Utilizing the test tank, the maximum amplitude resembles the case of the fixed velocity with 2000 iterations, but without small oscillations.

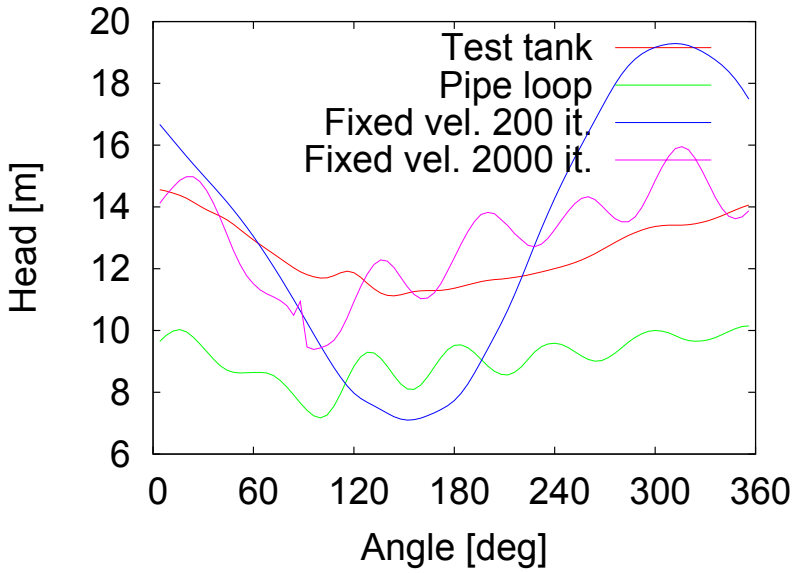

Fig. 4: Head as a function of the impeller angle in the time-accurate simulations with the test tank and the pipe loop geometries as well as the fixed velocity cases.

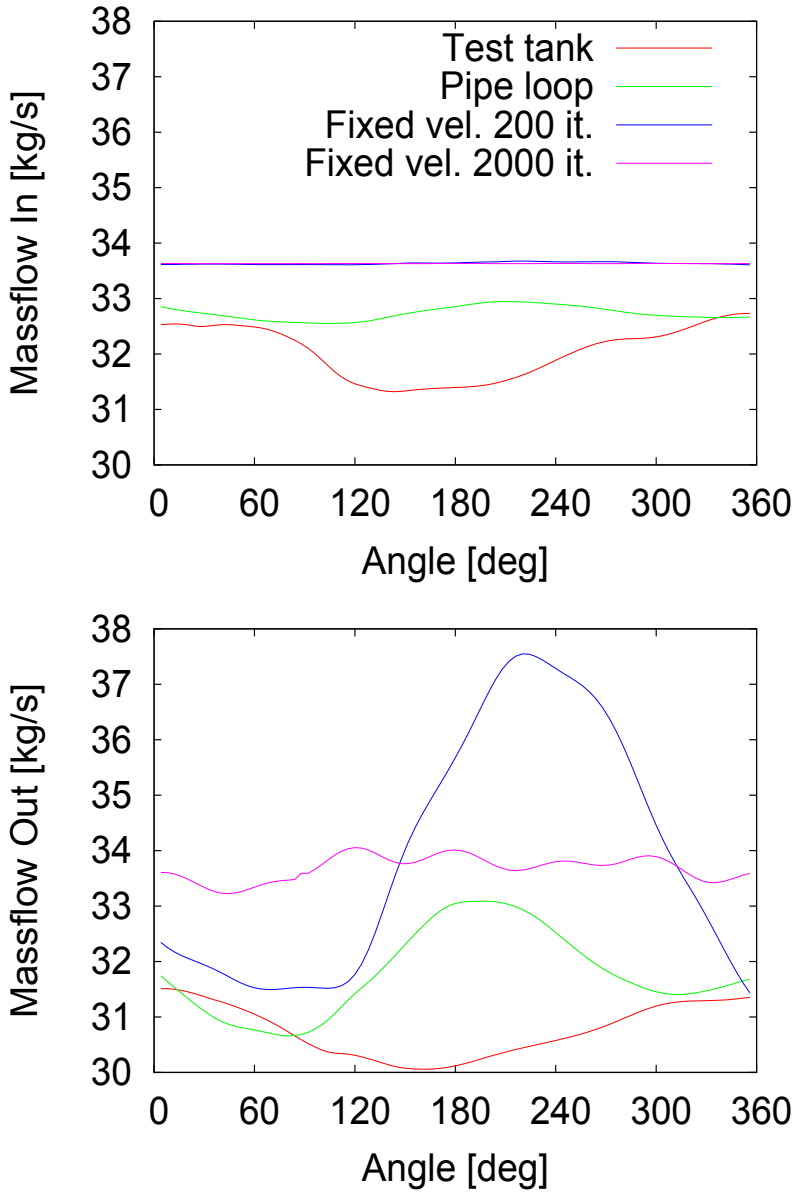

Fig. 5: Massflow in (top) and massflow out (bottom) as a function of the impeller angle in the time-accurate simulations with the test tank and the pipe loop geometries as well as the fixed velocity cases.

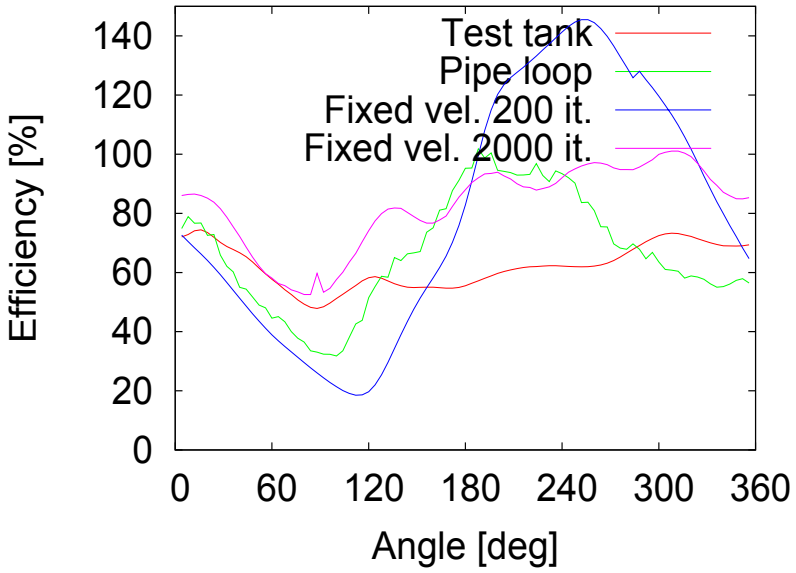

Fig. 6: The efficiency as a function of the impeller angle in the time-accurate simulations with the test tank and the pipe loop geometries as well as the fixed velocity cases.

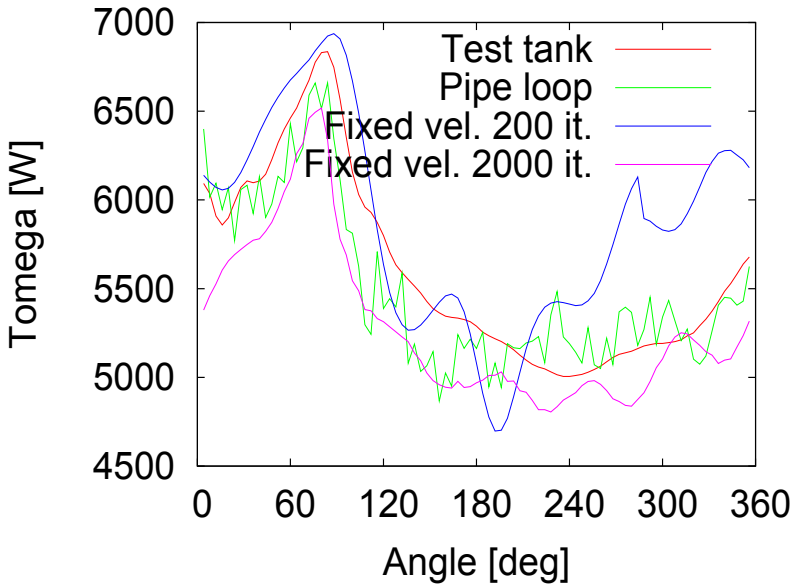

Fig. 7: The shaft power as a function of the impeller angle in the time-accurate simulations with the test tank and the pipe loop geometries as well as the fixed velocity cases.

The problem of fluctuating pressure is related to convergence problems. When a number of internal iterations is increased, pressure is changing lineary after first 50 iterations. And it continues changing, which was tested even with 30 000 iterations. But, opposite to one might expect, the amplitude of pressure fluctuations is smaller when iteration number is increased. On the other hand the number of pressure fluctuations per impeller revolution is increased. Convergence histories of average pressure and maximum pressure change within a timestep (2 000 internal iterations) are shown in Fig. 8.

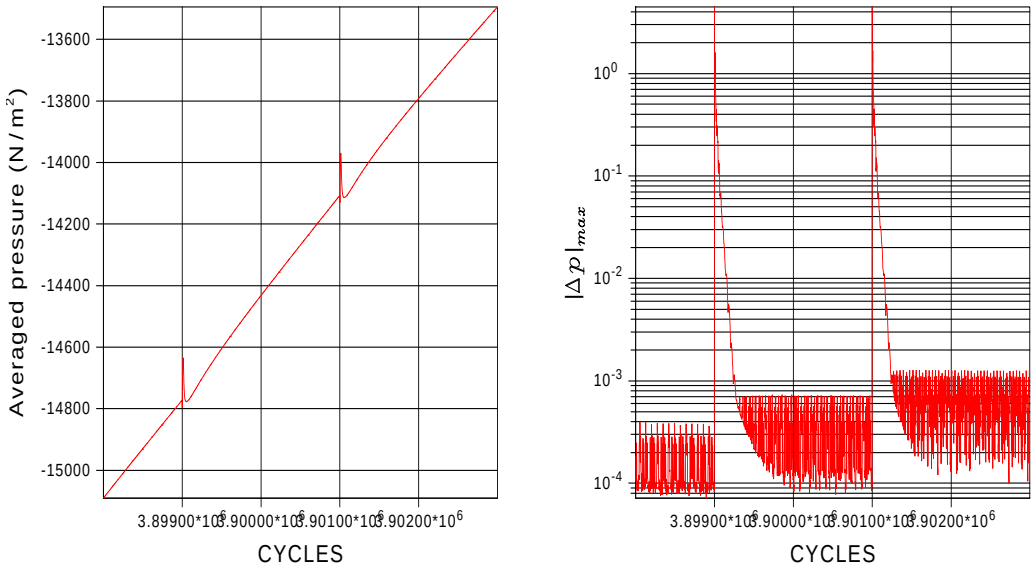

Fig. 8: Convergence history of average pressure (left) and maximum change of pressure (right) within a timestep.

Pressure distributions on the surface of the impeller and on a half of the volute, as well as velocity vectors and velocity distributions at the measurement stations, given in Fig. 9, are shown in Figs. A-1 – A-8 of Appendix A.

In velocity distributions there are no significant differences between the cases. Pressure distributions are quite different between the cases, and that is partly because secondary oscillations of the pressure are affecting the distribution quickly espesicially in case of 2 000 internal iterations.

Velocity vector distributions at the planes through measurement point 1 and an enlarged part of the plane are shown in Fig. A-9 and A-10 of Appendix A. When 2 000 internal iterations are made, the flow is more complex with a secondary vortex whereas the flow is quite similar in cases simulated with 200 or 400 internal iterations.

Distributions for the velocity and turbulent kinetic energy, taken on a plane at a distance of 40 mm from the bottom of the impeller, are shown in Figs. A-11 - A-14 of Appendix A. The velocity in the figures is in an inertial coordinate system. In the velocity distributions there are only small differencies between the fixed velocity cases. In the test tank case the flow field is smoother inside the impeller near the wake of the blade. Also the turbulent kinetic energy

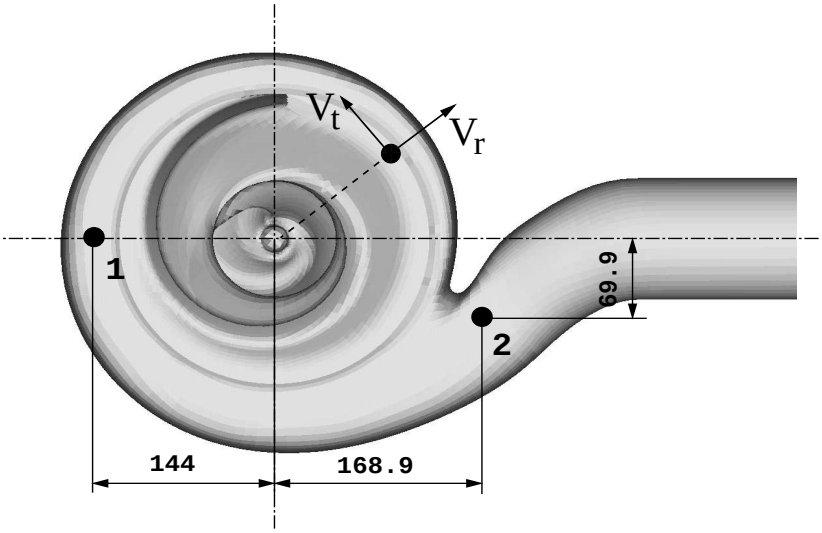

Fig. 9: Locations of the measurement points and directions of the tangential and radial velocities.

distribution of the test tank case is different from the others espesially in pressure side of the blade near the hub.

6 Discussion

In this study a single-blade sewage pump is simulated numerically using a low-Reynolds number $k - \epsilon$ turbulence closure. The purpose of the study was to investigate possible reasons for the numerical anomalies found with the simulations using the FINFLO code. The goal of the study was also to examine, how much a better convergence during the time step affects the error in the mass balance and also reflections from the outlet, which occur as unphysical pressure fluctuations. A test tank case without pressure fluctuations by nature was also simulated. A pipe loop case using similar outlet pipe area reduction was also tried. Unfortunately the pipe loop case results suffer from the fact that the non-matching boundary is reducing time-dependent nature of the flow.

With a highly oscillating flow in single blade pump simulation, boundary conditions play a significant role in pressure oskillations, but quantitative values as well as the velocity distributions are not affected so much. Velocity distributions were predicted with a good accuracy. Use of the test tank eliminated oscillations, but there are some problems conserving the massflow.

References

[1] Auvinen, M., "Computational Analysis of a Single-Blade Sevage Pump with FINFLO CFD/TERMO-51-2006, Unpublished," Helsinki University of Technology, Laboratory of Applied Thermodynamics, April 2006.

[2] *FINFLO User Guide, version 7.1.* Helsinki University of Technology, Finland, 2003.

[3] Rahman, M., Rautaheimo, P., and Siikonen, T., "Numerical Study of Turbulent Heat Transfer from a Confined Impinging Jet Using a Pseudo-compressibility Method," in *Proceedings of the 2nd International Symposium on Turbulence, Heat and Mass Transfer*, (Delft), pp. 511–520, June 1997.

[4] Hoffren, J., "A Numerical Method for Simulating Unsteady Flow Including Solid/Fluid Interaction," Helsinki University of Technology, Laboratory of Aerodynamics, 1995. ISBN 951–22–2759–2.

[5] Chien, K.-Y., "Predictions of Channel and Boundary-layer Flows with a Low-Reynolds-Number Turbulence Model," *AIAA Journal*, Vol. 20, No. 1, 1982, pp. 33–38.

A Distributions

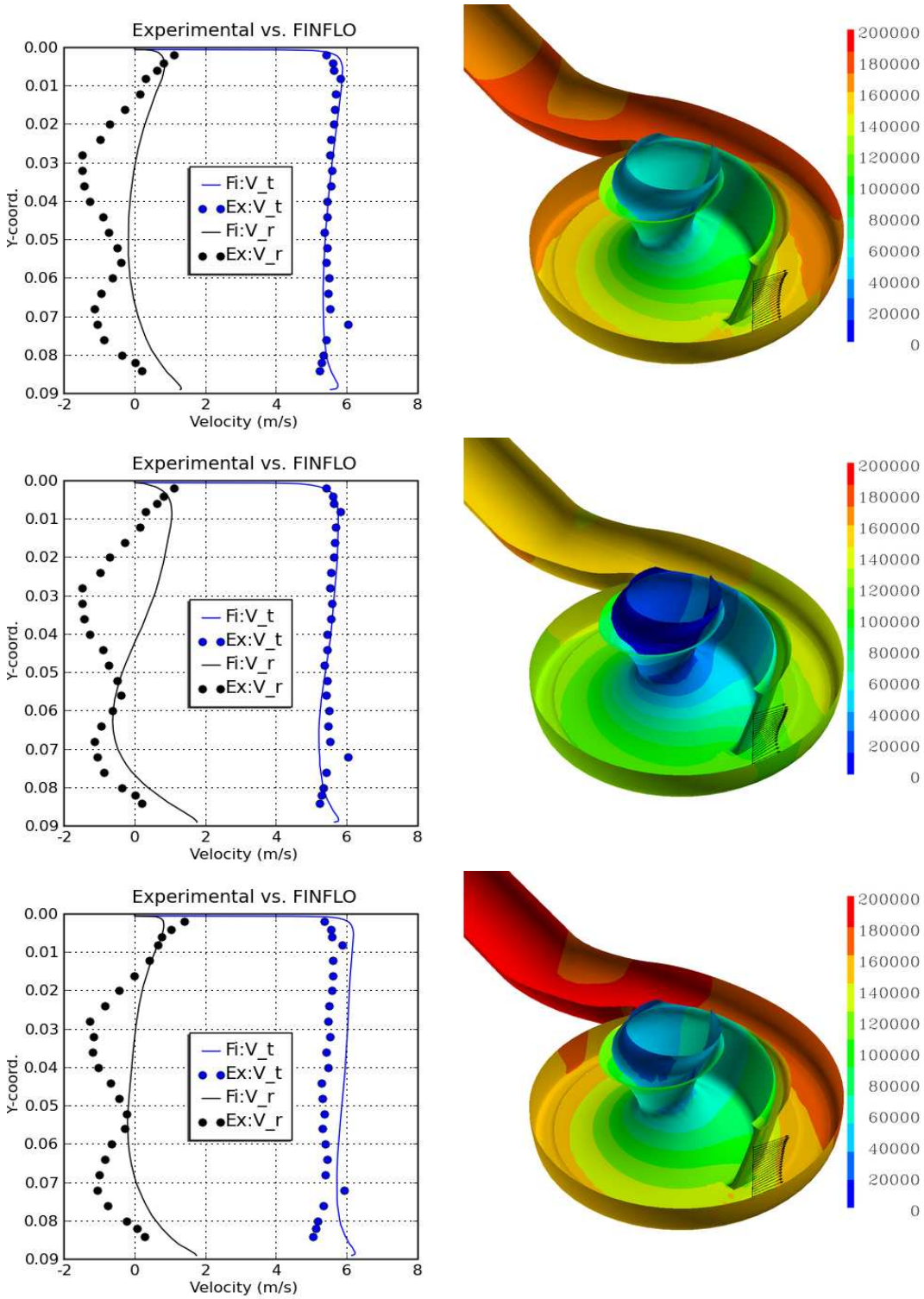

Fig. A-1: Pressure distribution on the surface of the impeller and volute, velocity vectors and velocity distributions at measurement point 1. From top to bottom: The fixed velocity boundary conditions with 200 internal iterations, with 2 000 internal iterations and the test tank case. The impeller angle is 0°.

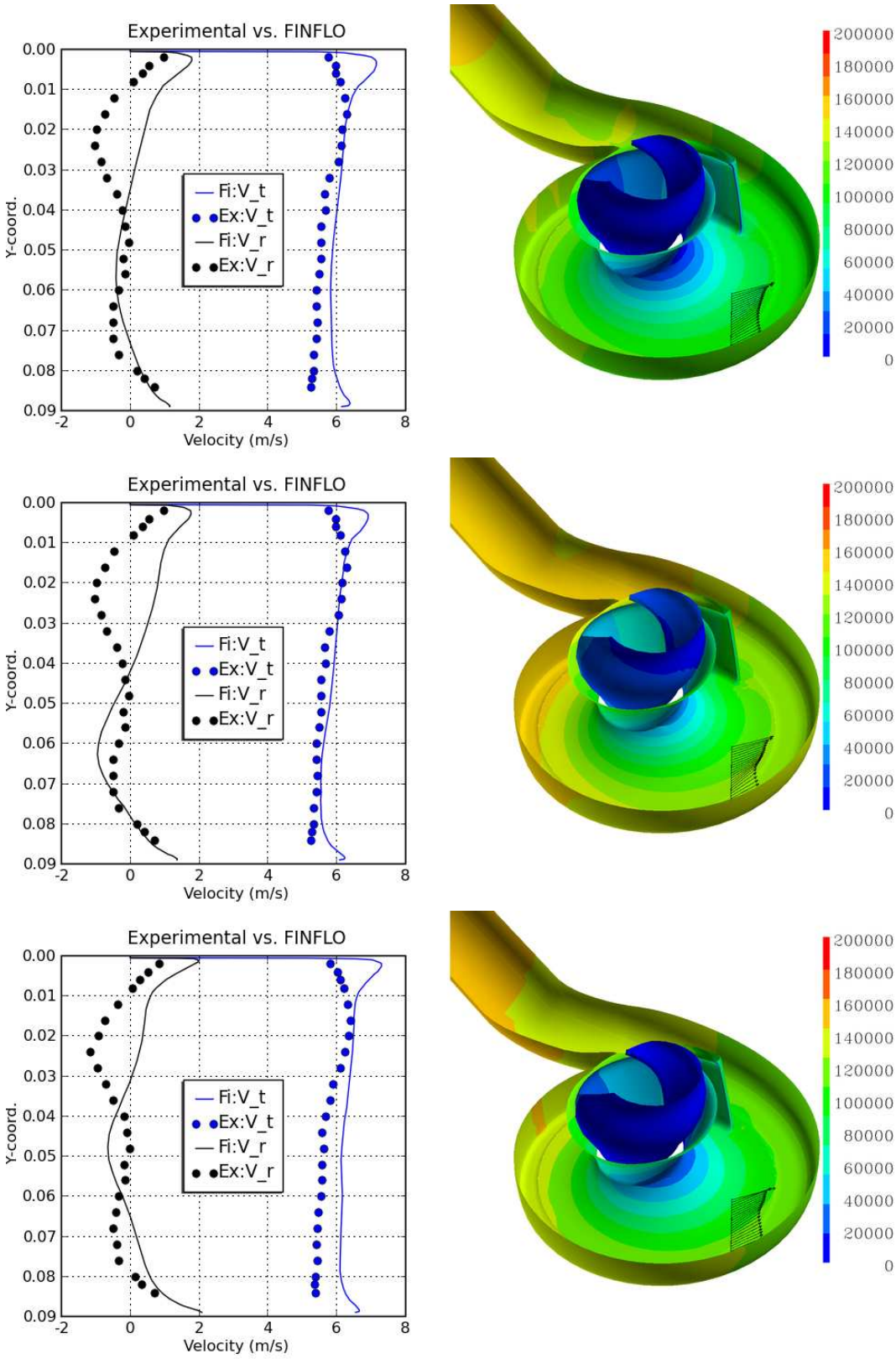

Fig. A-2: Pressure distribution on the surface of the impeller and volute, velocity vectors and velocity distributions at measurement point 1. The orientation as in Fig. A-1. The impeller angle is 90°.

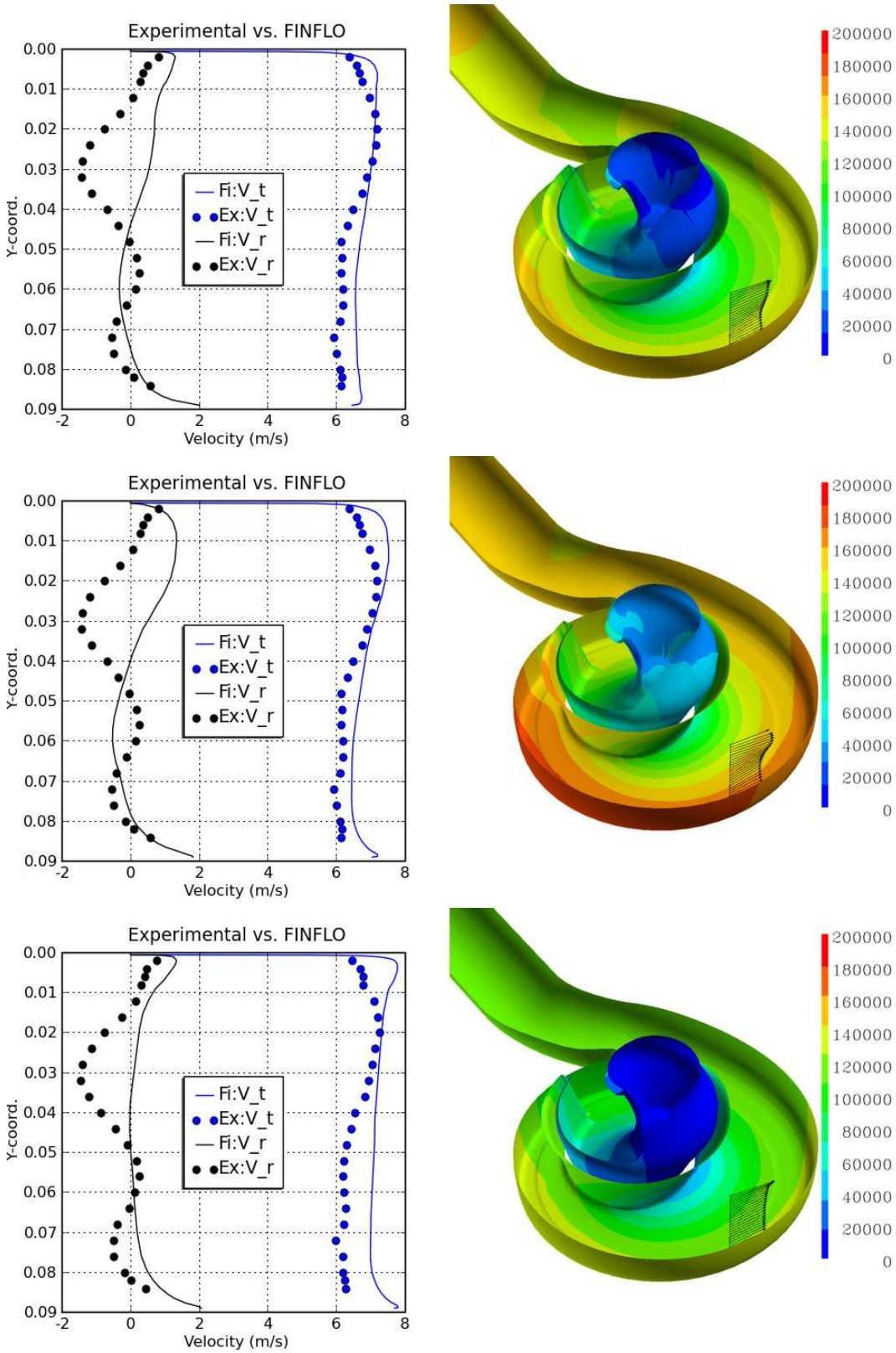

Fig. A-3: Pressure distribution on the surface of the impeller and volute, velocity vectors and velocity distributions at measurement point 1. The orientation as in Fig. A-1. The impeller angle is 180°.

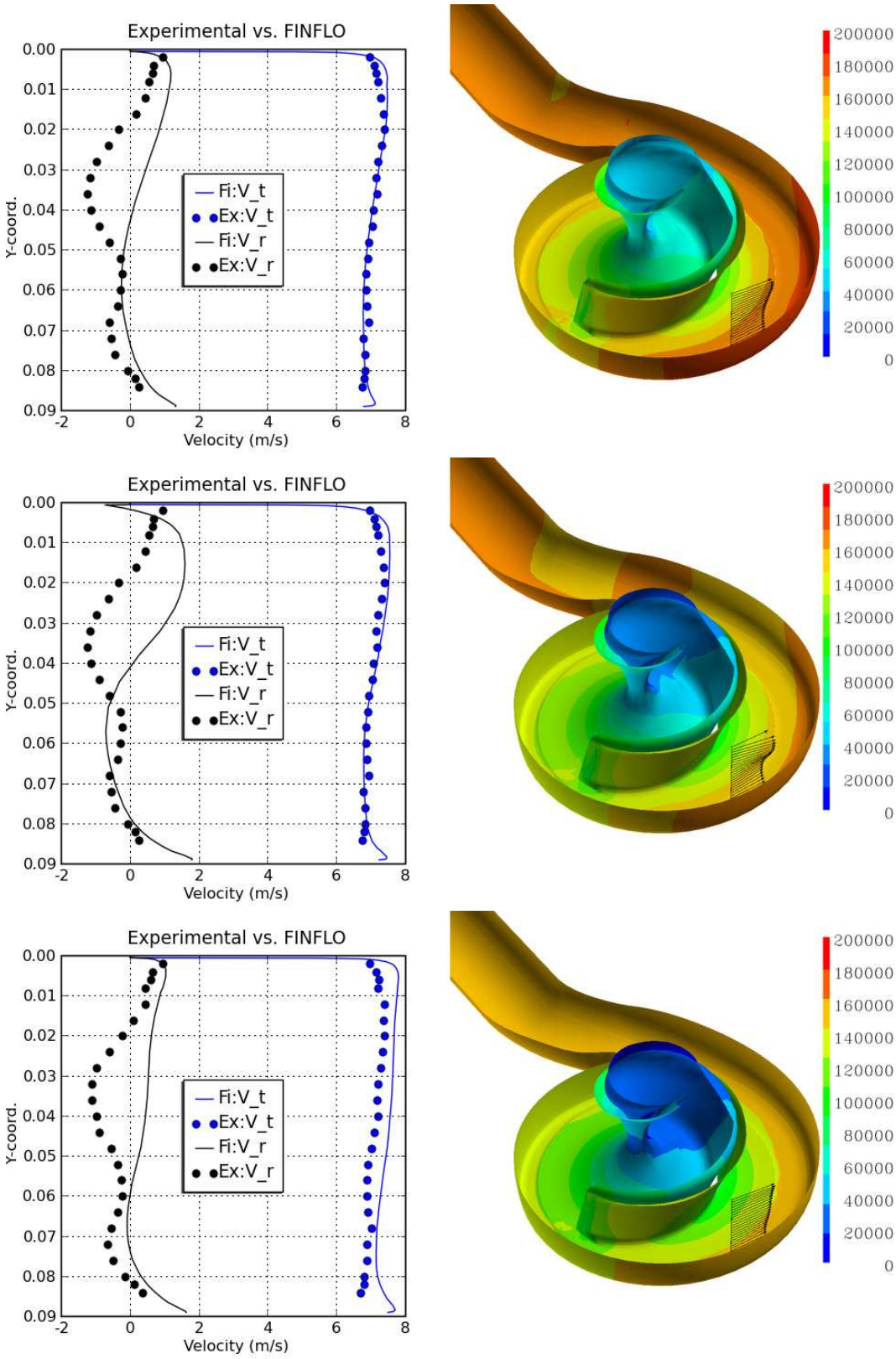

Fig. A-4: Pressure distribution on the surface of the impeller and volute, velocity vectors and velocity distributions at measurement point 1. The orientation as in Fig. A-1. The impeller angle is 270°.

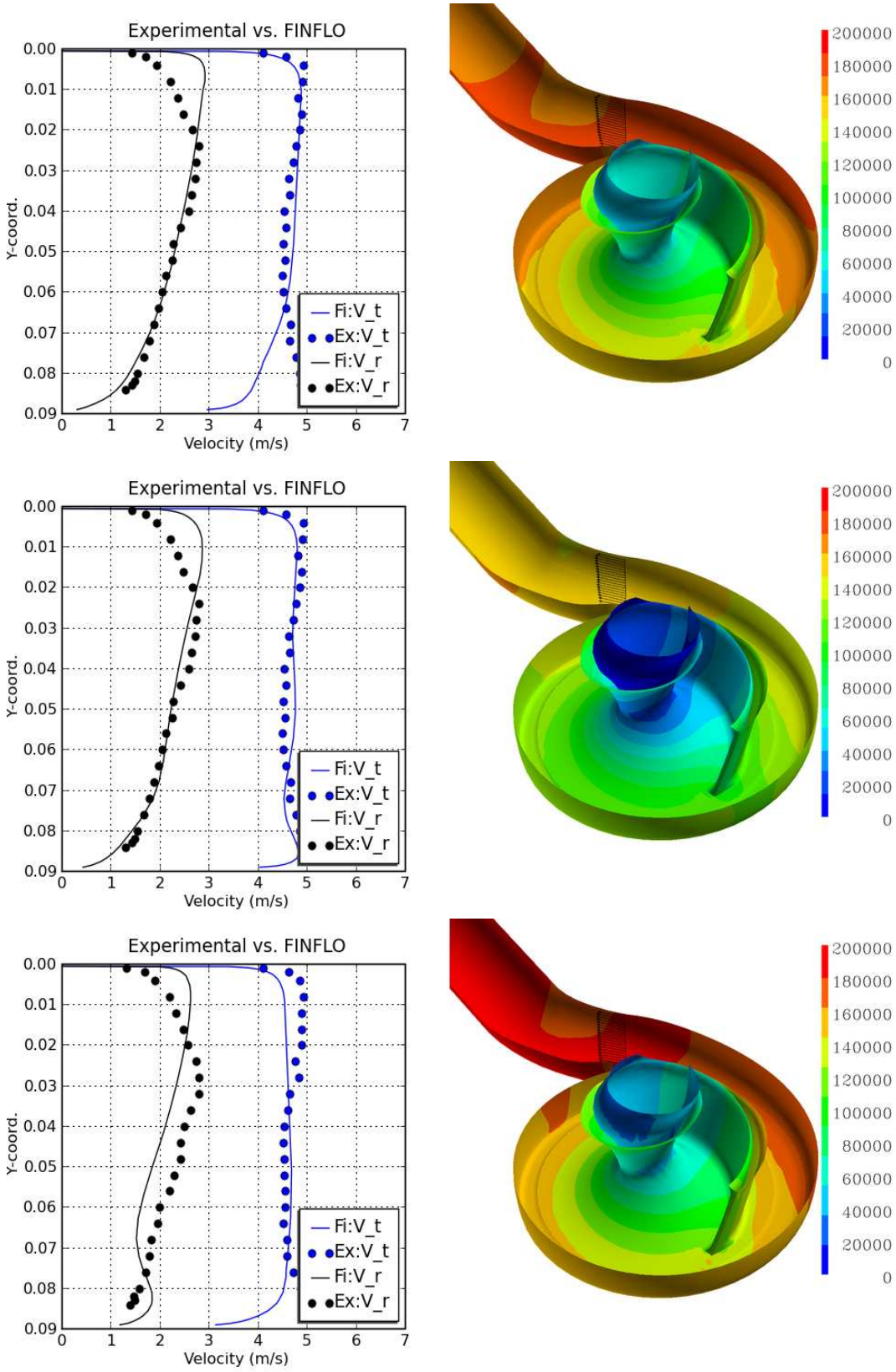

Fig. A-5: Pressure distribution on the surface of the impeller and volute, velocity vectors and velocity distributions at measurement point 2. The orientation as in Fig. A-1. The impeller angle is 0°.

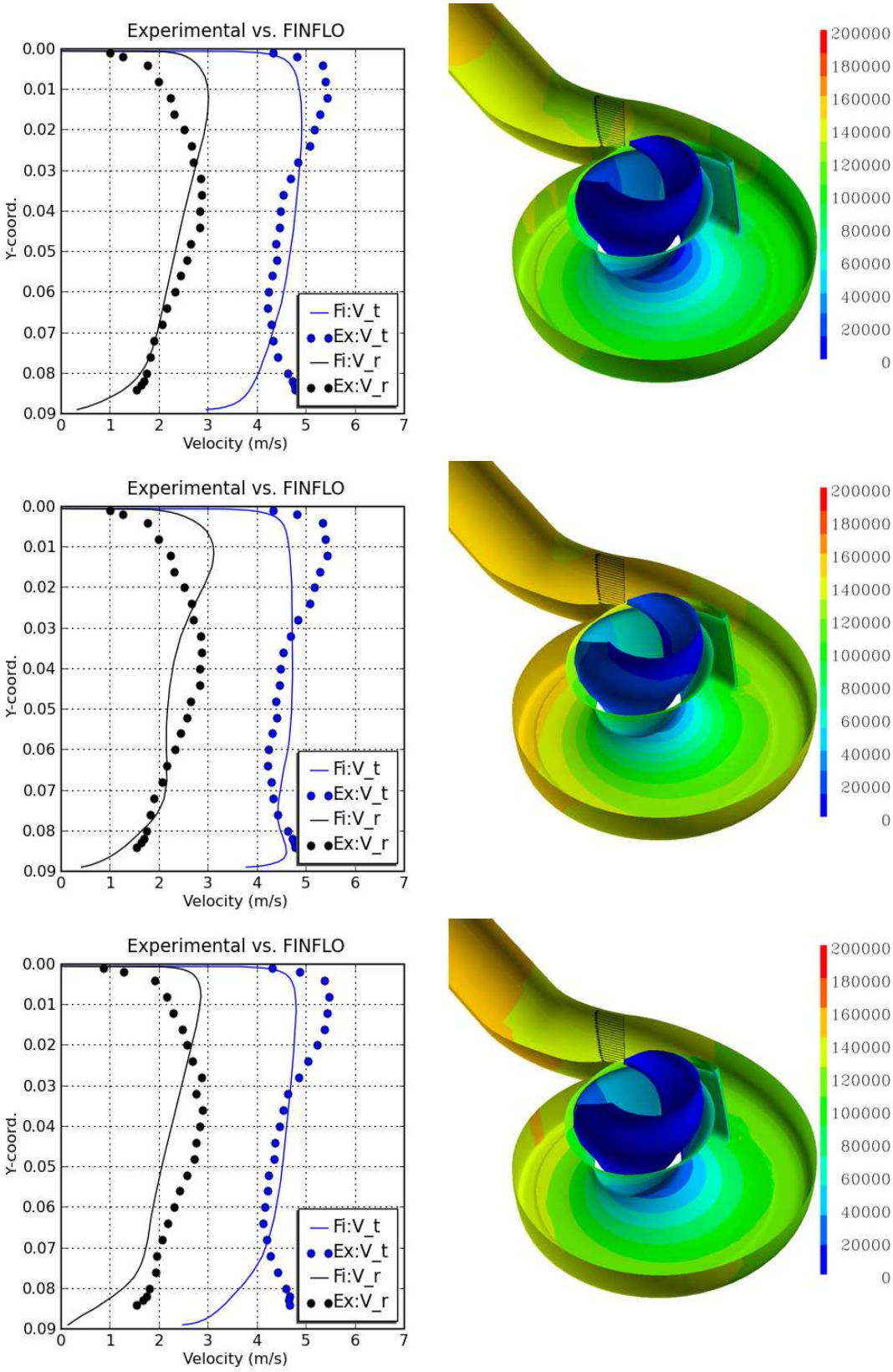

Fig. A-6: Pressure distribution on the surface of the impeller and volute, velocity vectors and velocity distributions at measurement point 2. The orientation as in Fig. A-1. The impeller angle is 90°.

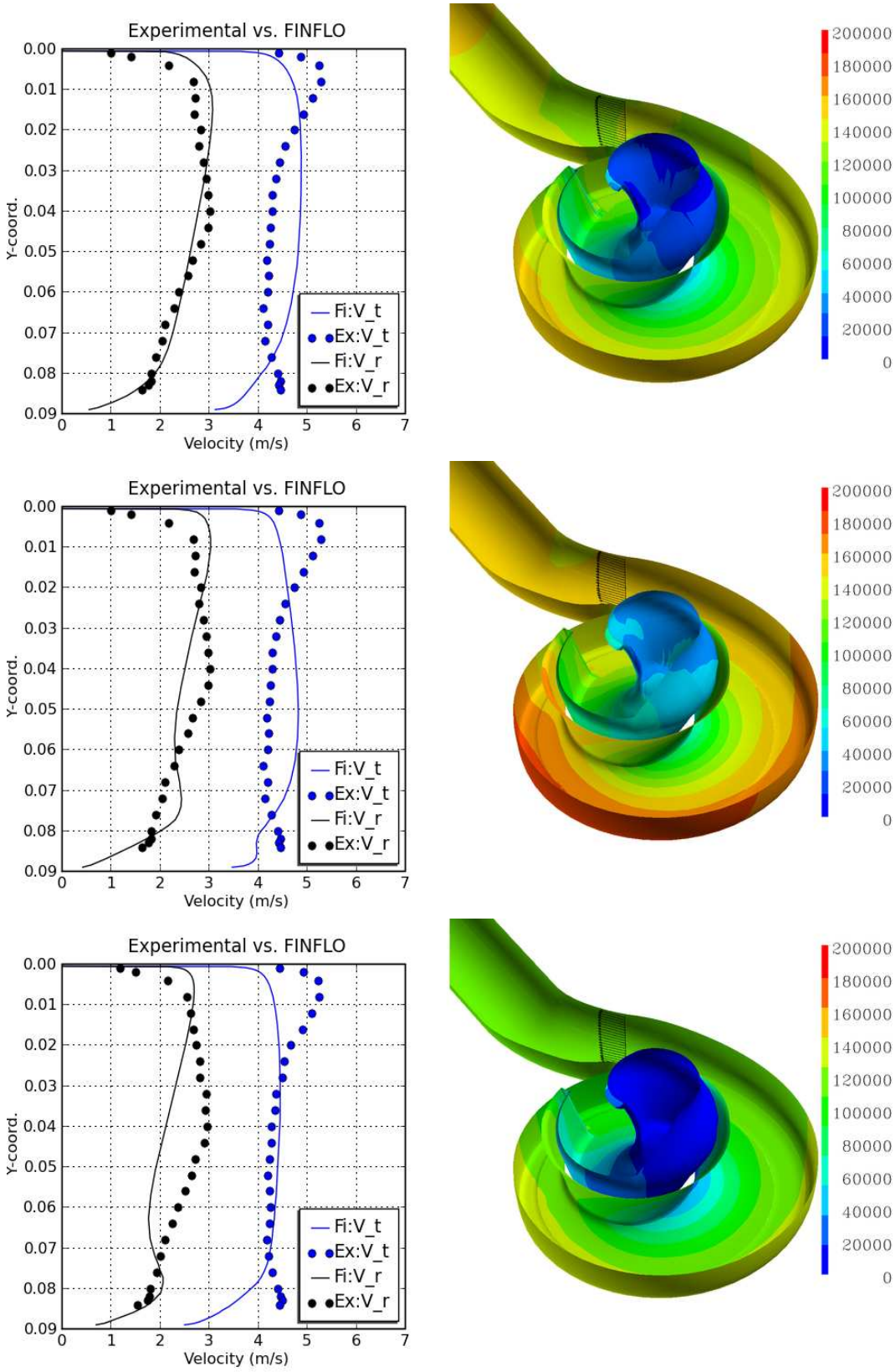

Fig. A-7: Pressure distribution on the surface of the impeller and volute, velocity vectors and velocity distributions at measurement point 2. The orientation as in Fig. A-1. The impeller angle is 180°.

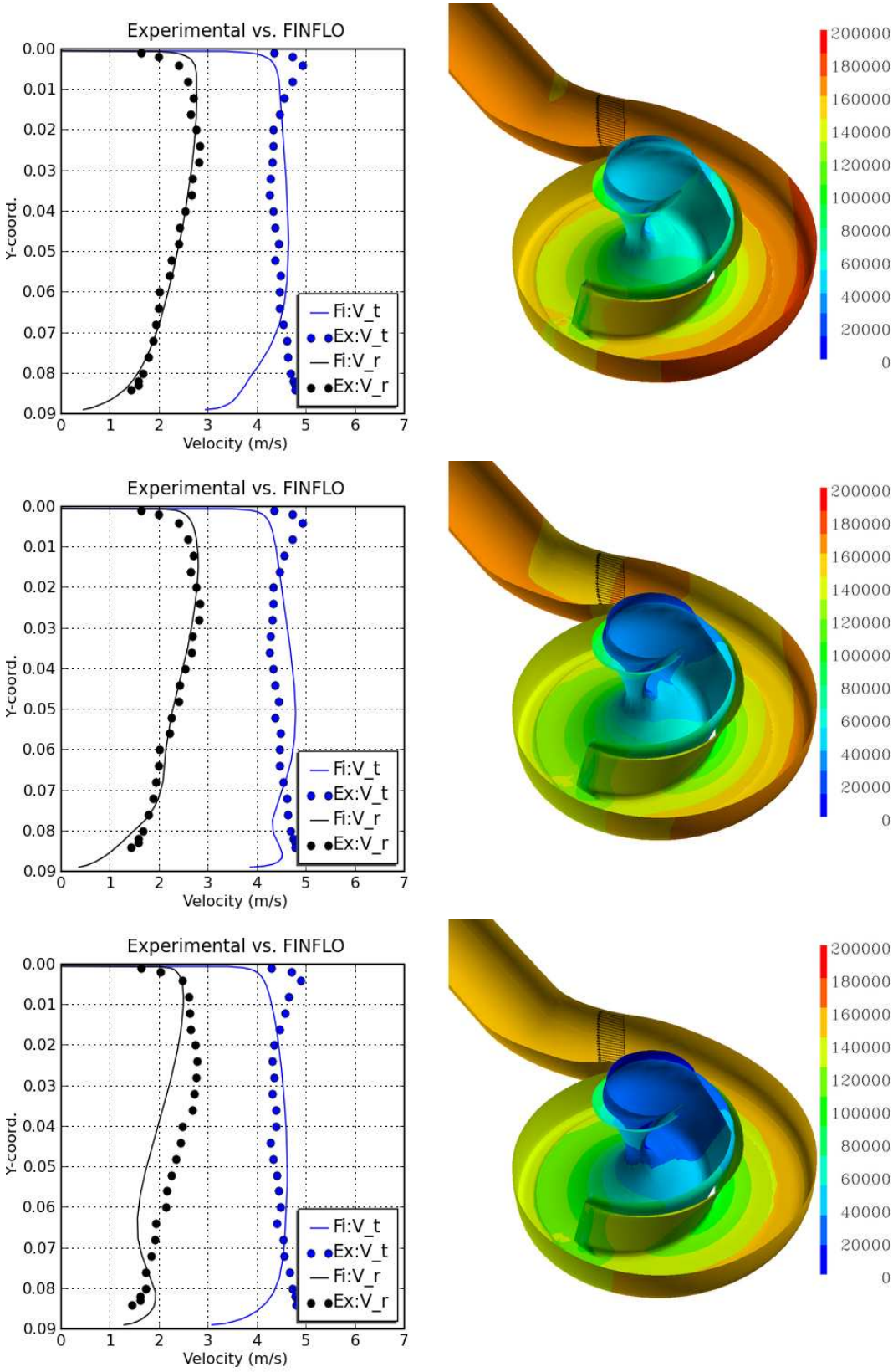

Fig. A-8: Pressure distribution on the surface of the impeller and volute, velocity vectors and velocity distributions at measurement point 2. The orientation as in Fig. A-1. The impeller angle is 270°.

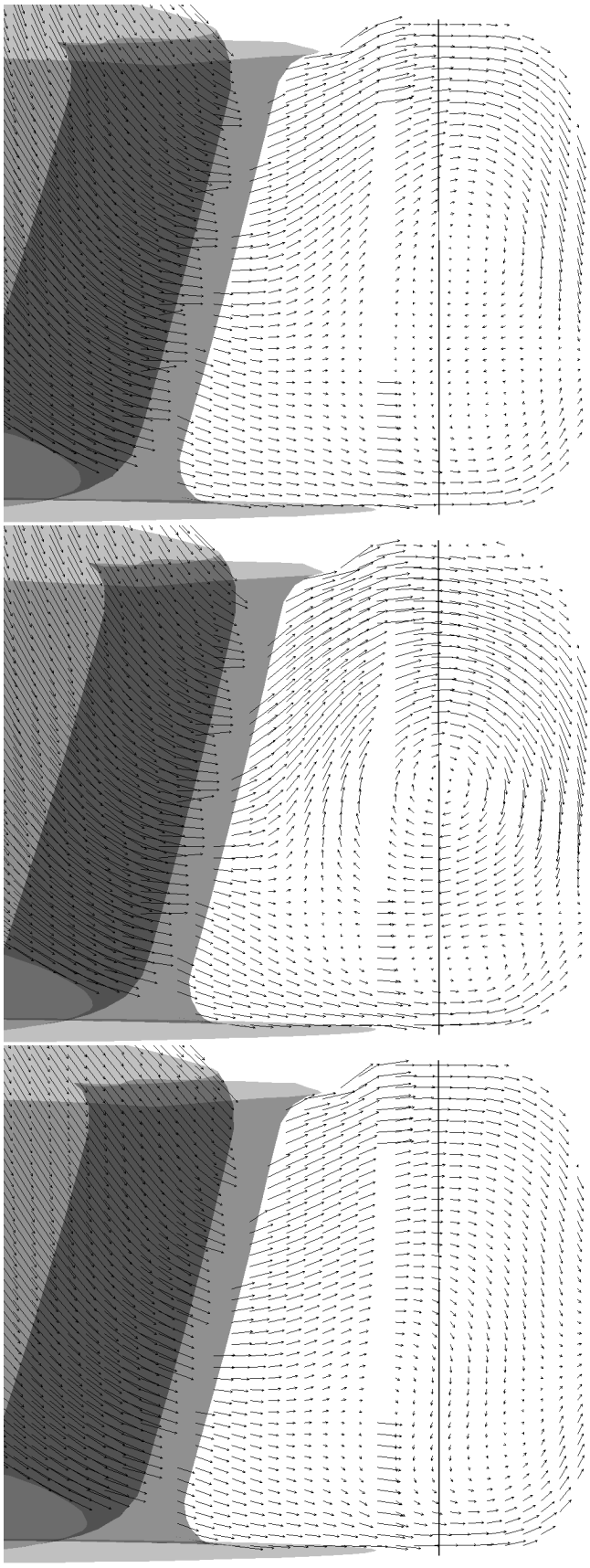

Fig. A-9: Projected velocity vectors in a plane from center of the impeller to measurement point 1. Fixed velocity case with 200 internal iterations (top), 2 000 internal iterations (middle) and the test tank case (bottom).

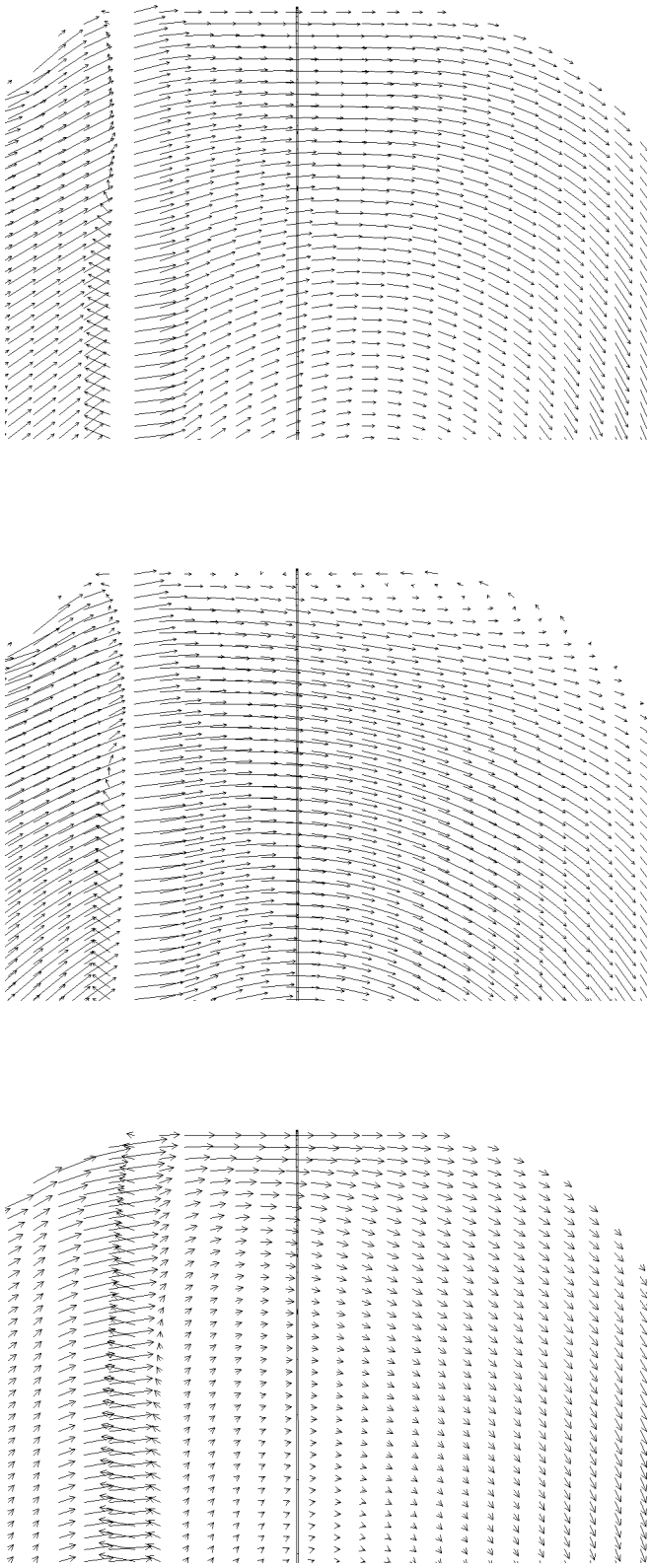

Fig. A-10: Projected velocity vectors in a plane from center of the impeller to measurement point 1 zoomed in to upper side of the volute. Fixed velocity case with 200 internal iterations (top), 2 000 internal iterations (middle) and the test tank case (bottom).

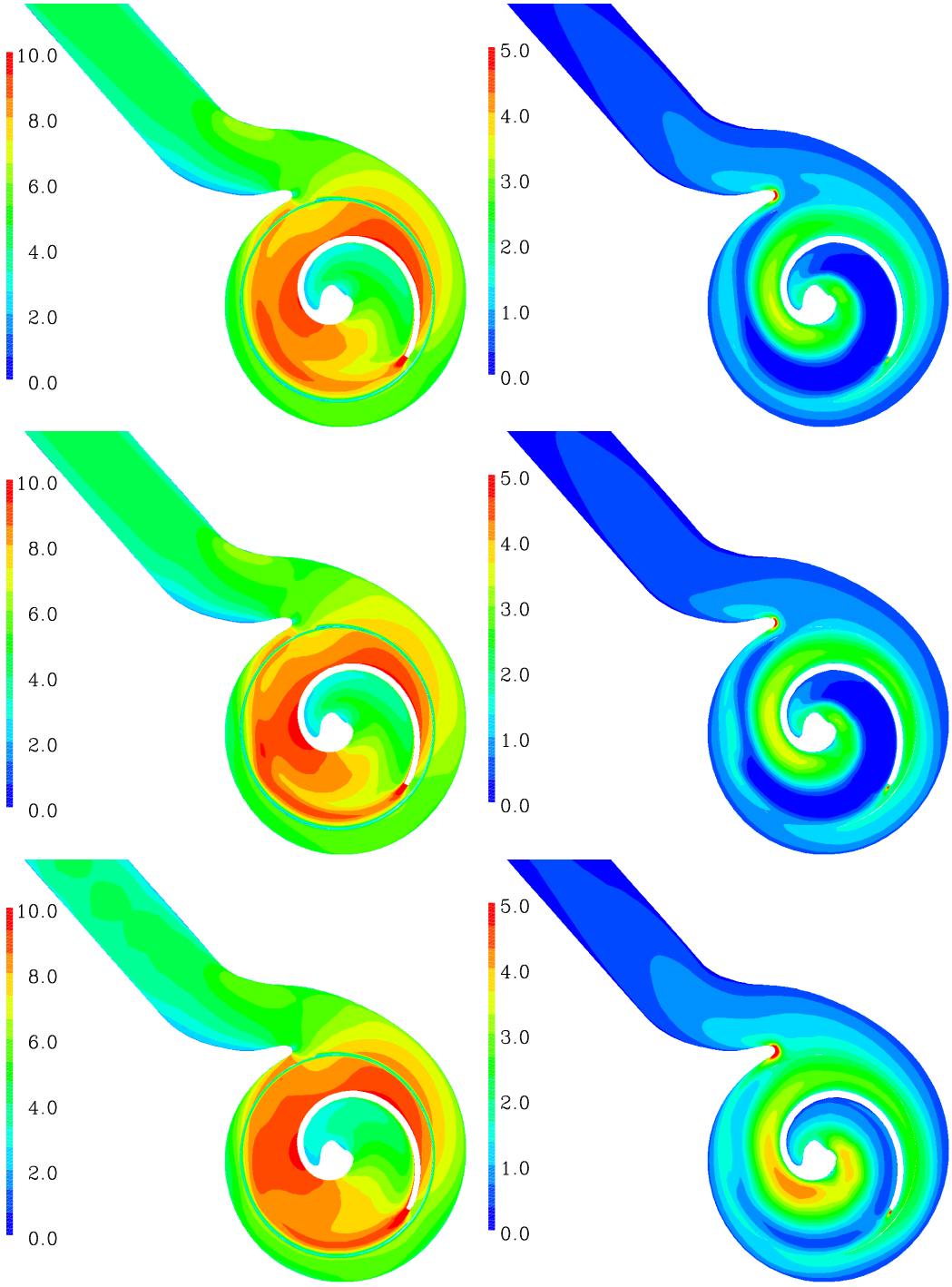

Fig. A-11: Distribution of velocity (left) and turbulent kinetic energy (right) at plane 40 mm from the bottom of the impeller. From top to bottom the fixed velocity boundary conditions with 200 internal iterations, with 2 000 internal iterations and the test tank case. The impeller angle is 0°.

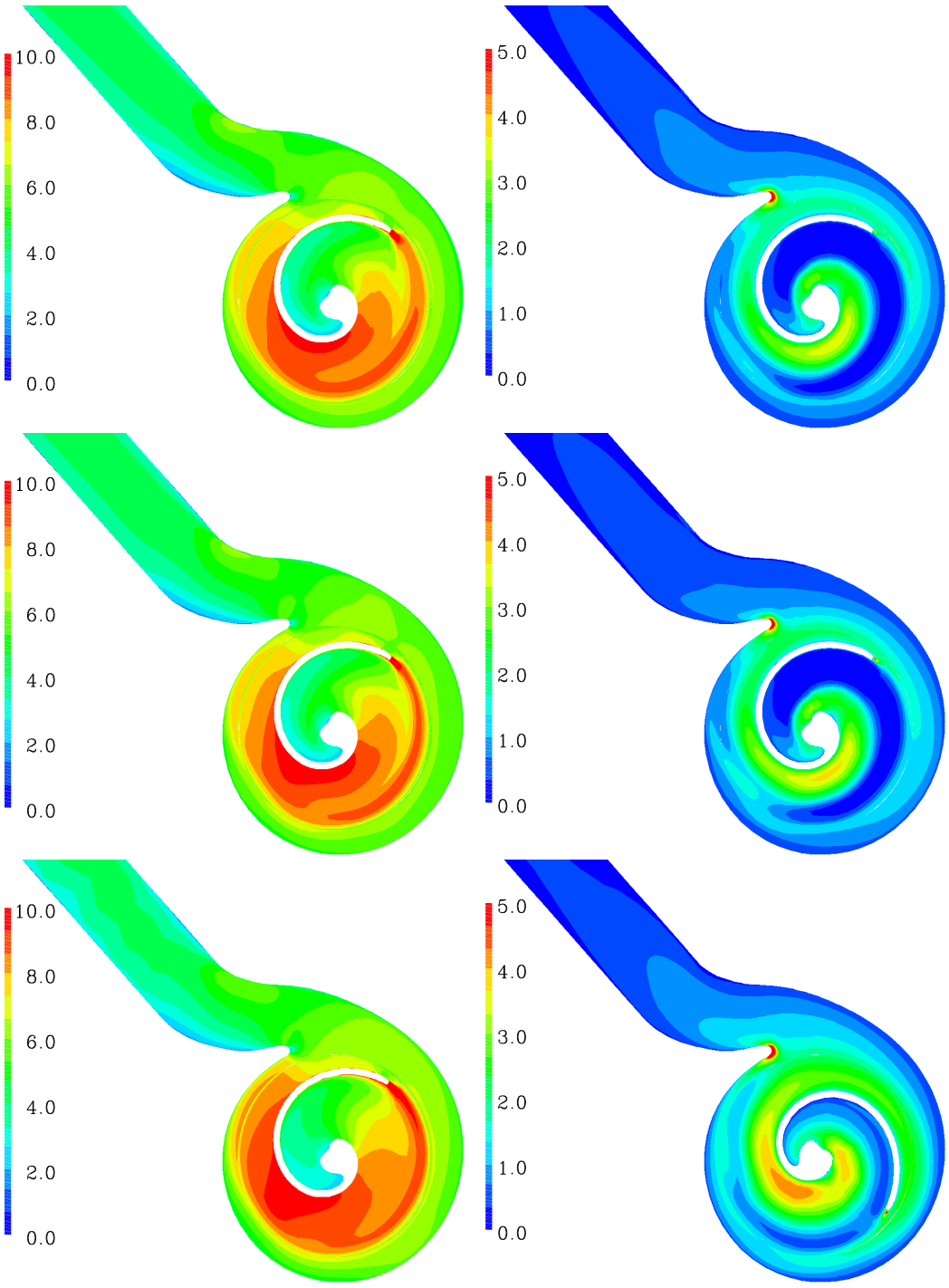

Fig. A-12: Distribution of velocity (left) and turbulent kinetic energy (right) at plane 40 mm from the bottom of the impeller. The orientation as in Fig. A-11. The impeller angle is 90°.

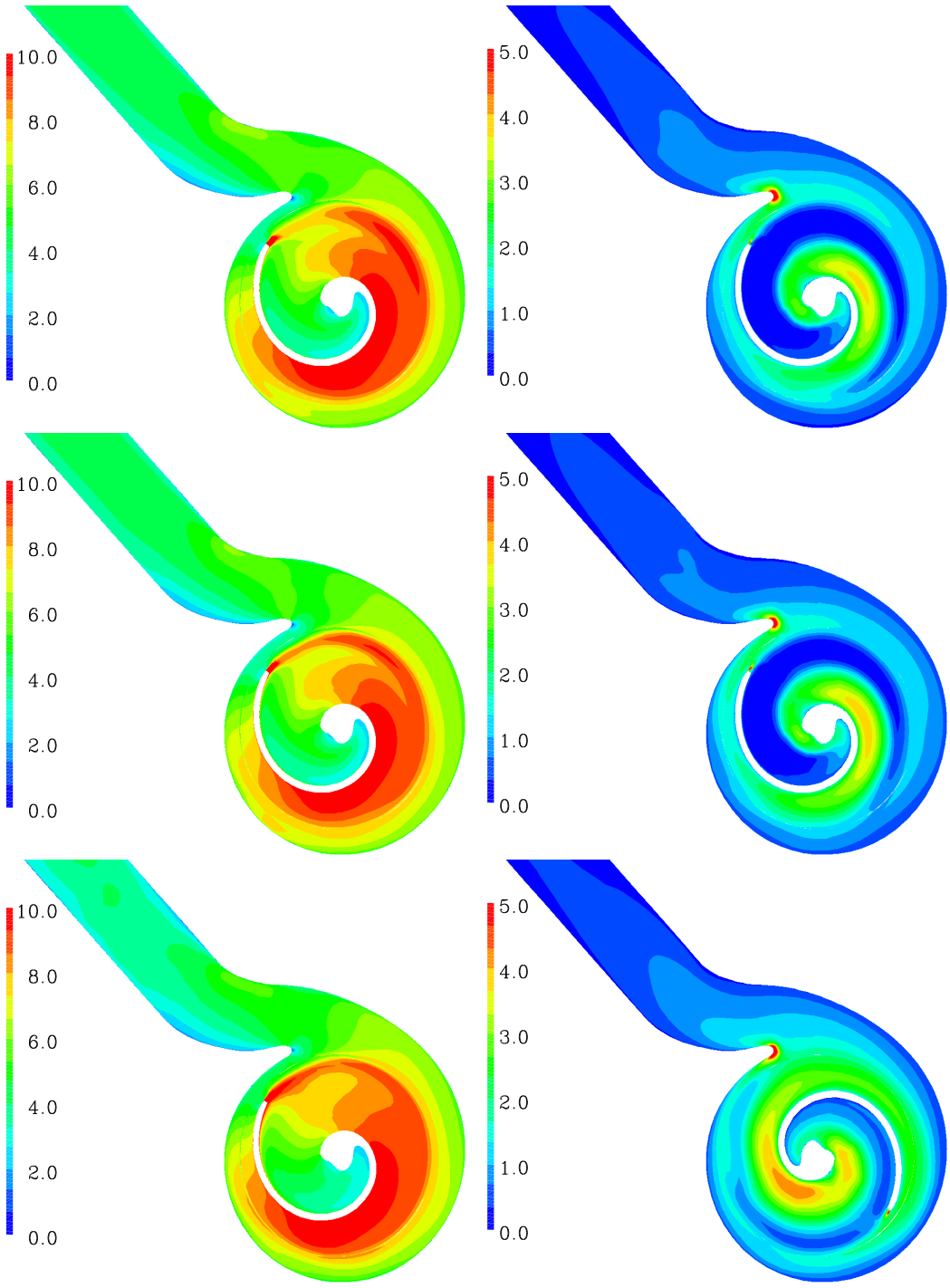

Fig. A-13: Distribution of velocity (left) and turbulent kinetic energy (right) at plane 40 mm from the bottom of the impeller. The orientation as in Fig. A-11. The impeller angle is 180°.

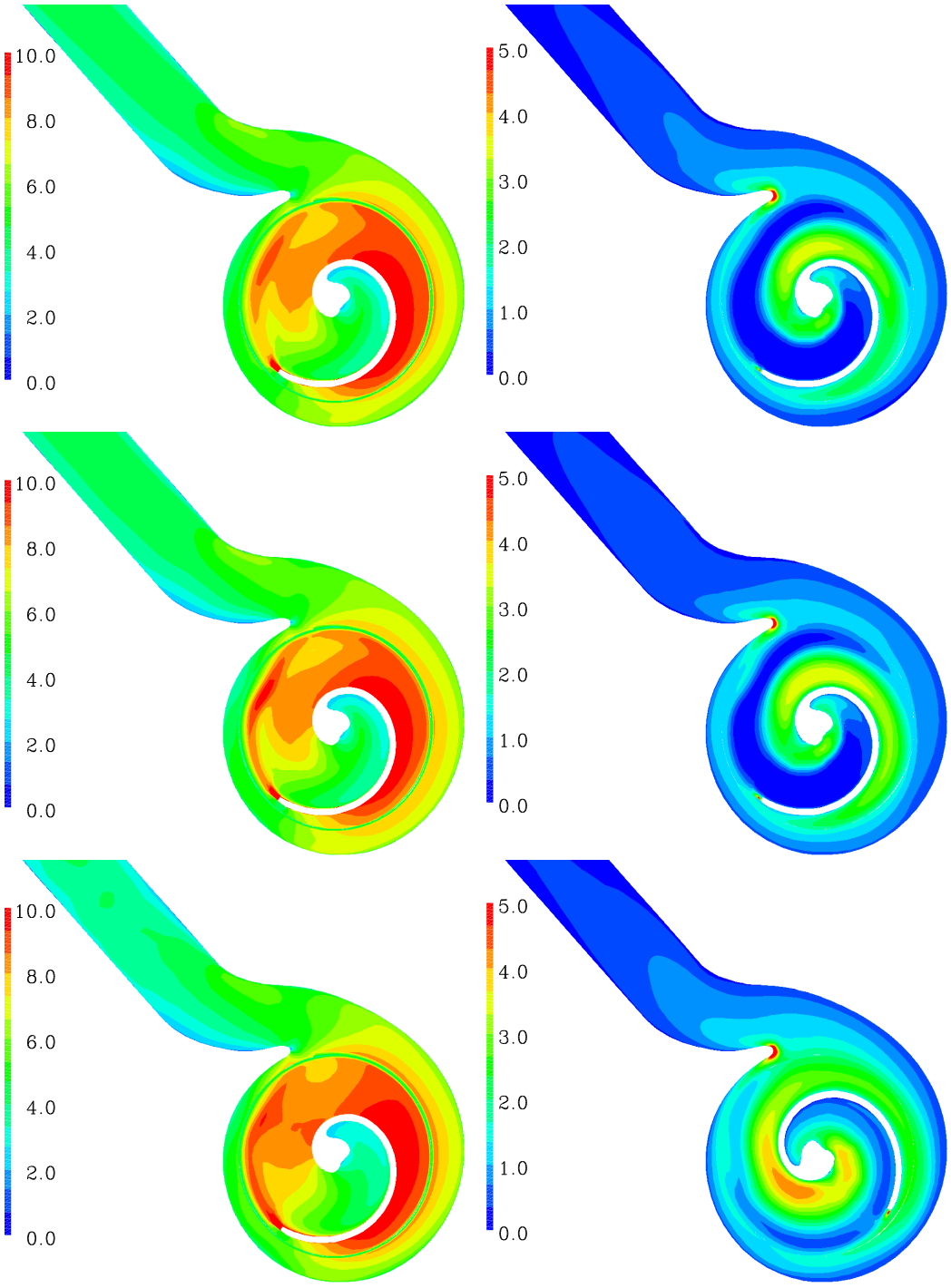

Fig. A-14: Distribution of velocity (left) and turbulent kinetic energy (right) at plane 40 mm from the bottom of the impeller. The orientation as in Fig. A-11. The impeller angle is 270°.